

pubs.acs.org/cm Article

# Cation Segregation in Alloyed Thiophosphates $Fe_{2-x}Co_xP_2S_6$

Matthew Cheng, Abishek K. Iyer, Alexios P. Douvalis, Stephanie M. Ribet, Mercouri G. Kanatzidis, and Vinayak P. Dravid\*



Cite This: Chem. Mater. 2023, 35, 1458-1465



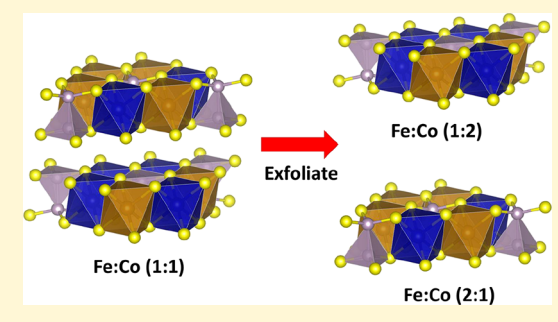
**ACCESS** 

Metrics & More

Article Recommendations

Supporting Information

**ABSTRACT:** Metal thiophosphates are a versatile class of van der Waals materials that can exhibit drastically different properties depending on the metal cations that are incorporated. Solid solutions between different members of this class are of interest to study due to the evolution of the magnetic, topological, and semiconductor properties in these materials. However, there has not yet been a thorough examination of the homogeneity of the cation species within the alloyed system of interest that may prove vital if these thiophosphates are to be incorporated into devices in conjunction with other van der Waals materials. Herein, we report on the structural and chemical differences between measurements of bulk and exfoliated  $Fe_{2-x}Co_xP_2S_6$ , which were synthesized with a  $P_2S_5$  flux method. In the bulk,



powder X-ray diffraction and scanning electron microscopy energy-dispersive X-ray spectroscopy indicate a homogeneous stoichiometry. This is corroborated by Mössbauer spectroscopy, which in addition suggests that as the quantity of Co introduced into the  $Fe_{2-x}Co_xP_2S_6$  structure increases, the probability of having the nearest neighbors of any given  $Fe^{2+}$  cation to be  $Co^{2+}$  cations is substantially increased. However, upon exfoliation of  $Fe_{2-x}Co_xP_2S_6$ , Raman spectroscopy and electron energy loss spectroscopy (EELS) measurements suggest that the composition of individual exfoliated flakes deviates significantly from the expected average stoichiometry, and the distribution of  $Fe^{2+}$  and  $Co^{2+}$  is not perfectly homogeneous.

## 1. INTRODUCTION

Ever since the discovery of graphene by Geim and Novoselov in 2004, there has been an abundance of activity in synthesizing new 2D van der Waals (vdW) materials and studies in their properties and applications. 1-4 vdW materials are of great interest as the vdW gap between individual monolayers offers a frame for the development of interesting anisotropic properties such as magnetic or transport to appear and also facilitates the isolation of individual monolayers. 5-One such vdW system is the metal chalcophosphates,  $M_2P_2X_6$ , M = transition metal, X = S, and Se (MCPs). The MCPs have drawn significant research interest for applications in catalysis, as cathode materials for batteries, and in next-generation nanoelectronics. 4,5,8-10 The MCPs adopt a monoclinic crystal structure and are composed of a [P<sub>2</sub>Q<sub>6</sub>]<sup>4-</sup> anion unit coordinated with a metal cation in an octahedral site. 4,5,11 The versatility of this class of vdW materials lies in the ability to incorporate many different cation species into the cation site as long as the overall charge balances with the  $[P_2Q_6]^{4-}$  anion unit. For example, Fe<sub>2</sub>P<sub>2</sub>S<sub>6</sub> is a well-studied Ising antiferromagnetic thiophosphate system with Fe being incorporated with a 2+ charge. 4,11-14 On the other hand, CuInP<sub>2</sub>S<sub>6</sub> is a layered room temperature ferroelectric thiophosphate system with Cu having a 1+ charge and In with a 3+ charge. 4,15 Furthermore, the  $[P_2Q_6]^{4-}$  lattice can also incorporate a wide range of metal cations into the remaining two-thirds of octahedral sites. For example, the Mg2+ in Mg2P2S65 has an

ionic radius of 72 pm $^{16}$  while the Ag $^{1+}$  and In $^{3+}$  in AgInP $_2S_6^{17}$  have ionic radii of 115 and 80 pm, respectively.  $^{16}$ 

This capability of incorporating different metal cations also enables the MCPs to be easily alloyed. By alloying different metal cations into the same system, the exhibited properties of the MCPs can be tuned by chemical substitution. For example, both Ni<sub>2</sub>P<sub>2</sub>S<sub>6</sub> and Mn<sub>2</sub>P<sub>2</sub>S<sub>6</sub> are antiferromagnetic systems with Néel temperatures of 155 and 78 K, respectively, with different magnetic anisotropies determined by the cation species that is incorporated. 13,18 Ni<sub>2</sub>P<sub>2</sub>S<sub>6</sub> has a predominantly in-plane alignment of the magnetic moments on the cation sites, while Mn<sub>2</sub>P<sub>2</sub>S<sub>6</sub> has a predominantly out-of-plane-alignment of magnetic moments on the cation sites. 13,18 Studies on Mn<sub>2-x</sub>Ni<sub>x</sub>P<sub>2</sub>S<sub>6</sub> show a distinct change in the Néel temperature and the three-dimensional ordering of the magnetic moments.<sup>18</sup> It has also been shown in multiple studies that more than two cation components can be alloyed together in the socalled high entropy alloy (HEA) chalcophosphates. 19-21 In these HEA chalcophosphates, up to five different metal cations can be alloyed into a single system. In the studies of these

Received: December 18, 2022 Revised: January 15, 2023 Published: February 2, 2023





alloyed MCPs, both bimetallic and HEA, the crystal structure and stoichiometry of the systems are evaluated and confirmed primarily by powder X-ray diffraction (pXRD) and scanning electron microscopy energy-dispersive X-ray spectroscopy (SEM-EDS) on bulk crystals or powdered bulk samples.<sup>1</sup> In all of these studies, the measurements from bulk samples indicate that a homogeneous solid alloy has been formed. However, it could be possible that the as-synthesized bulk samples may not be a homogeneous solid solution. It has been shown previously by Susner et al. that by varying the Cu/In ratio in  $CuInP_2S_6$ , a distinct phase segregation into  $CuInP_2S_6$  regions and  $In_{4/3}P_2S_6$  regions will result. Is, 25 It may very well be the case that other alloyed transition MCPs may also present phase segregation. This is an important consideration if these alloyed MCPs are to be used in next-generation nanoelectronics as the exfoliated flakes may in fact have different compositions than those expected from the bulk

Motivated by these considerations, we performed a followup study to a recent publication on a flux grown Fe<sub>2-x</sub>Co<sub>x</sub>P<sub>2</sub>S<sub>6</sub> system.<sup>26</sup> We applied a top-down approach to study the compositional changes at different length scales from bulk to exfoliated crystals of Fe<sub>2-x</sub>Co<sub>x</sub>P<sub>2</sub>S<sub>6</sub> using pXRD, SEM-EDS, Mössbauer spectroscopy (MS), Raman spectroscopy, and electron energy loss spectroscopy (EELS). First, the pXRD and SEM-EDS measurements on bulk samples were conducted to verify the expected structural and compositional evolution as the Fe/Co ratio is changed. From the MS measurements, separate Fe-rich and Co-regions were determined to be present simultaneously in all alloyed samples. This was further confirmed with the Raman analysis of exfoliated flakes, which showed a distinct compositional change in all alloyed samples, with the FeCoP<sub>2</sub>S<sub>6</sub> member showing the largest variation with flakes on the order of ~200 nm in thickness with lateral dimensions in the micron range showing Co-rich flakes and Ferich flakes. Finally, from the EELS analysis of selected alloyed samples, a distinct change within thin exfoliated flakes from bulk FeCoP<sub>2</sub>S<sub>6</sub> shows that Fe-rich and Co-rich regions are present even on the order of  $\sim$ 5 nm separation. This study emphasizes the importance of evaluating the structure and composition at multiple scales to achieve a more fundamental understanding of these materials impacting applications from catalysis with exfoliated bulk samples to incorporation of exfoliated flakes into 2D heterostructure devices.

#### 2. EXPERIMENTAL METHODS

2.1. Synthesis of  $Fe_{2-x}Co_xP_2S_6$ . The compounds were synthesized using the reactive P2S5 flux method, which is described in the paper by Chica et al. 12 The M (M/M') to P<sub>2</sub>S<sub>5</sub> ratios were 2:3 and 1:1:3 for the monometallic and bimetallic thiophosphates, respectively. In a nitrogen-filled glovebox, metal and P2S5 powders were loaded into 12.7 mm outer diameter and 10.5 mm inner diameter fused silica tubes with a total charge mass of 2 g. The amounts used are tabulated in Table S1 in the Supporting Information. The tubes were sealed with an oxy/natural gas torch under a pressure of  $\sim 3 \times 10^{-3}$  mbar. After sealing, the tubes were mechanically agitated for 10 min to ensure mixing of the reagents. The tubes were heated using a computer-controlled tube furnace with the heating profiles, as shown in Table S2. The synthesis of Co<sub>2</sub>P<sub>2</sub>S<sub>6</sub> was performed at 580 °C to avoid the Co(PS) impurity at higher temperatures. Details of this can be found in the reference by Chica et al. 12 Lebail fit was performed for quantitative pXRD analysis to confirm phase purity (Figure S1). Warning: The removal of the flux must be performed in a fume hood as this reaction releases H<sub>2</sub>S gas. In a fume hood, the silica ampoule was opened, and the ingot was

placed in a 20 mL scintillation vial with 10 mL of a 50/50 vol:vol mixture of DI water and ethanol (50/50  $H_2\mathrm{O:EtOH})$  and heated to  $\sim\!70$  °C for 1 h. If any flux remained, the solution was decanted and 10 mL of 50/50  $H_2\mathrm{O:EtOH}$  was added and heated for 1 h. After removing the flux, the product was washed twice with DI water and acetone. The residual thiols were left to off-gas overnight.

- **2.2. Powder X-ray Diffraction (pXRD).** The pXRD patterns of  $Fe_{2-x}Co_xP_2S_6$  (x=0-1.75) were collected on a Rigaku Miniflex 600 diffractometer with a Cu K $\alpha$  source operating at 40 kV and 15 mA with a K $\beta$  filter. The preferred orientation was reduced by sieving the lightly ground samples to a particle size of <53  $\mu$ m and using a welled, zero background sample holder. The data collection was performed at a rate of 5°/min.
- **2.3. Scanning Electron Microscopy Energy-Dispersive X-ray Spectroscopy (SEM-EDS).** Scanning electron microscopy energy-dispersive X-ray spectroscopy (SEM-EDS) was conducted with a Hitachi SU8030 with an Oxford AZtec X-max 80 SDD EDS detector. EDS spectra were analyzed with Oxford Aztec software.
- **2.4.** Mössbauer Spectroscopy (MS).  $^{57}$ Fe Mössbauer spectra (MS) were collected in transmission geometry at sample temperatures of 300 and 77 K using constant-acceleration spectrometers, equipped with  $^{57}$ Co(Rh) sources kept at RT, in combination with a liquid N<sub>2</sub> bath (Oxford Instruments Variox 760) Mössbauer cryostat. Metallic  $\alpha$ -Fe at RT was used for the velocity calibration of the spectrometers, and all isomer shift (IS) values were given relative to this standard. The experimentally recorded MS were fitted and analyzed using the IMSG code.  $^{27}$
- 2.5. Electron Energy Loss Spectroscopy (EELS) Analysis. Electron energy loss spectroscopy (EELS) spectral imaging (SI) mapping was conducted using a JEOL ARM200 with a Gatan K2 Direct electron detector. The ARM200 was operated at 200 kV, 15  $\mu$ A emission current with a convergence angle of 27.1 mrad, and an EELS spectrometer collection angle of 83 mrad. It was necessary to scan quickly to prevent beam damage to the sample with a pixel time of 2.5 ms.

## 3. RESULTS AND DISCUSSION

After synthesizing the selected members of the Fe<sub>2-x</sub>Co<sub>x</sub>P<sub>2</sub>S<sub>6</sub> series as described in Section 2.1, the crystal structure and chemical homogeneity were evaluated at multiple length scales using a top-down approach as the Fe and Co concentrations are varied. To understand the bulk structure and composition, pXRD, SEM-EDS, and Raman spectroscopy were used. The crystal symmetry is determined along with the unit cell parameters as a function of alloying in the bulk from the pXRD, and the alloying ratio of Fe:Co is determined from SEM-EDS and Raman spectroscopy. However, these measurements do not capture potential nanoscale perturbations, so Mössbauer spectroscopy (MS), a more local interrogation technique, was used to assess the average ordering of the nearest neighbor cation species relative to the Fe cation species. A distinct evolution of the MS as a function of Coalloying indicates the presence of Fe-rich and Fe-poor phase segregated regions. This is corroborated with additional Raman analysis on the exfoliated flakes of Fe<sub>2-x</sub>Co<sub>x</sub>P<sub>2</sub>S<sub>6</sub>, indicating a significant variation in the alloying composition beginning with flakes that are on the order of hundreds of nanometers in thickness. To directly map the nanoscale perturbations of Fe and Co, thin exfoliated flakes approaching ~10 nm in thickness are evaluated with scanning transmission electron microscopy (STEM) using EELS and these observations show composition fluctuations present in the intralayer separated by 5 nm.

**3.1. Structural Analysis - pXRD.** As has been previously reported, both  $\text{Fe}_2\text{P}_2\text{S}_6$  and  $\text{Co}_2\text{P}_2\text{S}_6$  are monoclinic with the space group C2/m. As shown in Figure 1a, the thiophosphates are composed of a  $[\text{P}_2\text{S}_6]^{4-}$  anion unit

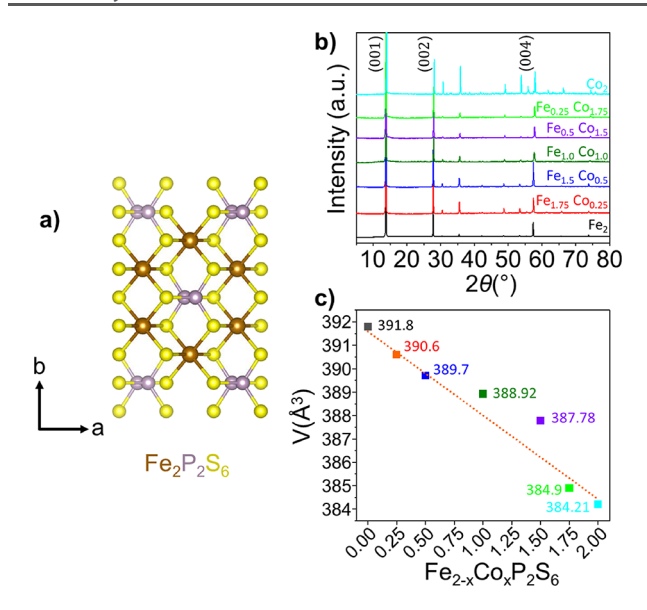


**Figure 1.** (a) Schematic representation of the  $Fe_2P_2S_6$  lattice. (b) pXRD patterns for  $Fe_{2-x}Co_xP_2S_6$ . (c) Calculated cell volumes for all  $Fe_{2-x}Co_xP_2S_6$  from refinements of pXRD patterns.

coordinated around a metal cation in an octahedral site. 11 We have reported previously that the alloyed Fe<sub>2-x</sub>Co<sub>x</sub>P<sub>2</sub>S<sub>6</sub> system also crystallizes as C2/m and closely follows Vegard's law where the addition of more cobalt is shown to shift  $2\theta$  to a higher value, indicating a more relaxed structure.<sup>26</sup> With the addition of two more alloyed thiophosphate systems, Fe<sub>0.5</sub>Co<sub>1.5</sub>P<sub>2</sub>S<sub>6</sub> and Fe<sub>1.5</sub>Co<sub>0.5</sub>P<sub>2</sub>S<sub>6</sub>, the structural analysis of all alloyed Fe2-xCoxP2S6 is conducted with pXRD. From the pXRD measurements, it is clear that the desired alloyed Fe<sub>2-x</sub>Co<sub>x</sub>P<sub>2</sub>S<sub>6</sub> systems were obtained, as seen in Figure 1b. Note that all diffraction patterns are normalized to the most intense peak corresponding to the (001) plane. As expected, the (00l) planes correspond to the most intense diffractogram peaks due to the layered nature of the alloyed Fe2-xCoxP2S6 systems. Some variations in the relative intensities of the corresponding diffraction peaks are expected as there is a difference in orientation of the powdered samples under measurement. All cell constants obtained from the pXRD refinement (Figure S1) are reported in Table S2. With greater amounts of Co alloyed, the cell volume decreases in approximate accordance with Vegard's law and our previous study.26 From the selected refinements of the alloyed  $Fe_{2-x}Co_xP_2S_6$  systems, the presence of the impurity phase CoP<sub>x</sub>S<sub>2-x</sub>, which readily forms when attempting to grow Co containing thiophosphates, is not observed. 12 To further corroborate that the alloyed Fe2-xCoxP2S6 systems are correctly synthesized in the bulk, SEM-EDS measurements of bulk Fe<sub>2-x</sub>Co<sub>x</sub>P<sub>2</sub>S<sub>6</sub> systems were conducted. Normalized bulk SEM-EDS spectra, as shown in Figure S2, reveal an expected gradual decrease in intensity of the Fe K $\alpha$  peak at 6.398 keV and a corresponding increase in intensity of the Co K $\alpha$  peak at 6.924 keV as the Co content of Fe<sub>2-x</sub>Co<sub>x</sub>P<sub>2</sub>S<sub>6</sub> is increased. However, it should be noted that the Fe K $\beta$  peak residing at 7.057 keV is only 0.128 eV higher than the Co K $\alpha$  peak at 6.924 keV. This may potentially increase the measured intensity of the Co K $\alpha$  peak during processing and increase the error in the relative stoichiometry measured. To circumvent this, the pure Fe<sub>2</sub>P<sub>2</sub>S<sub>6</sub> sample is used as a standard and the Fe K $\alpha$  peak is compared with the S K $\alpha$  peak to determine the

experimentally derived compositions of the  $Fe_{2-x}Co_xP_2S_6$  systems in comparison to the expected values (Figure S3).

**3.2. Structural Analysis** - **MS.** Having established the crystalline nature of the alloyed  $Fe_{2-x}Co_xP_2S_6$  with pXRD, it is of interest to determine the ordering of the  $Fe^{2+}$  and  $Co^{2+}$  cations with respect to the  $[P_2S_6]^{4-}$  lattice. All of the samples were measured at room temperature and then cooled and measured at 77 K (Figure 2). First, a wide velocity scale

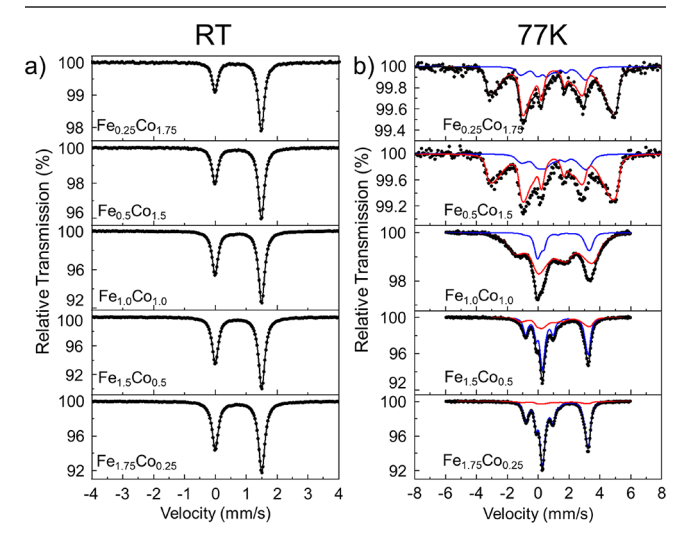


**Figure 2.** Mössbauer spectra of alloyed  $Fe_{2-x}Co_xP_2S_6$  samples recorded at (a) room temperature and (b) 77 K. The points correspond to the experimental data and the continuous lines to the components used to fit the spectra.

measurement at RT was carried out to confirm that no additional magnetic impurities are present that can contribute to the spectra and influence the results. As can be observed in Figure S4, no such impurities were observed. Moving to a narrower velocity scale, as can be seen in Figure 2a, all alloyed Fe2-xCoxP2S6 samples give almost identical spectra corresponding to a single contribution of Fe<sup>2+</sup> high spin character (S = 2) and Mössbauer parameters of nearly identical values for each sample (Table S3). The fit for the Fe<sup>2+</sup> with high spin character is shown as a black curve. Interestingly, in the  $FeCoP_2S_6$  and  $Fe_{1.75}Co_{0.25}P_2S_6$  samples, a small contribution from the Fe2+ low spin state could be also included in the fitting model. The appearance of this low spin state has been previously reported to manifest in layered systems.<sup>28-30</sup> However, this contribution is negligible ( $\leq$ 1% in absorption area) and does not affect the overall results.

The presence of nearly identical Mössbauer parameters for all the Fe<sup>2+</sup> ions in all the alloyed samples indicates that regardless of the composition of the Fe<sub>2-x</sub>Co<sub>x</sub>P<sub>2</sub>S<sub>6</sub> layered structure, the immediate first cation neighbor chemical environment of the Fe<sup>2+</sup> cations does not influence the local structure of the corresponding FeS<sub>6</sub> octahedra. Furthermore, it is interesting to note that the RT spectra exhibit no broadening of the resonant lines as the stoichiometry is changed. These results indicate that neither the local or global structure is altered by the alloying Fe/Co ratio and more specifically that the local environment of the Fe<sup>2+</sup> cation does not contribute significant distortions concerning the local structure as the Co content is increased. The results also reveal that there are negligible cation vacancies in the structure as the Fe<sup>2+</sup> cations are replaced with corresponding Co ions, which means that the

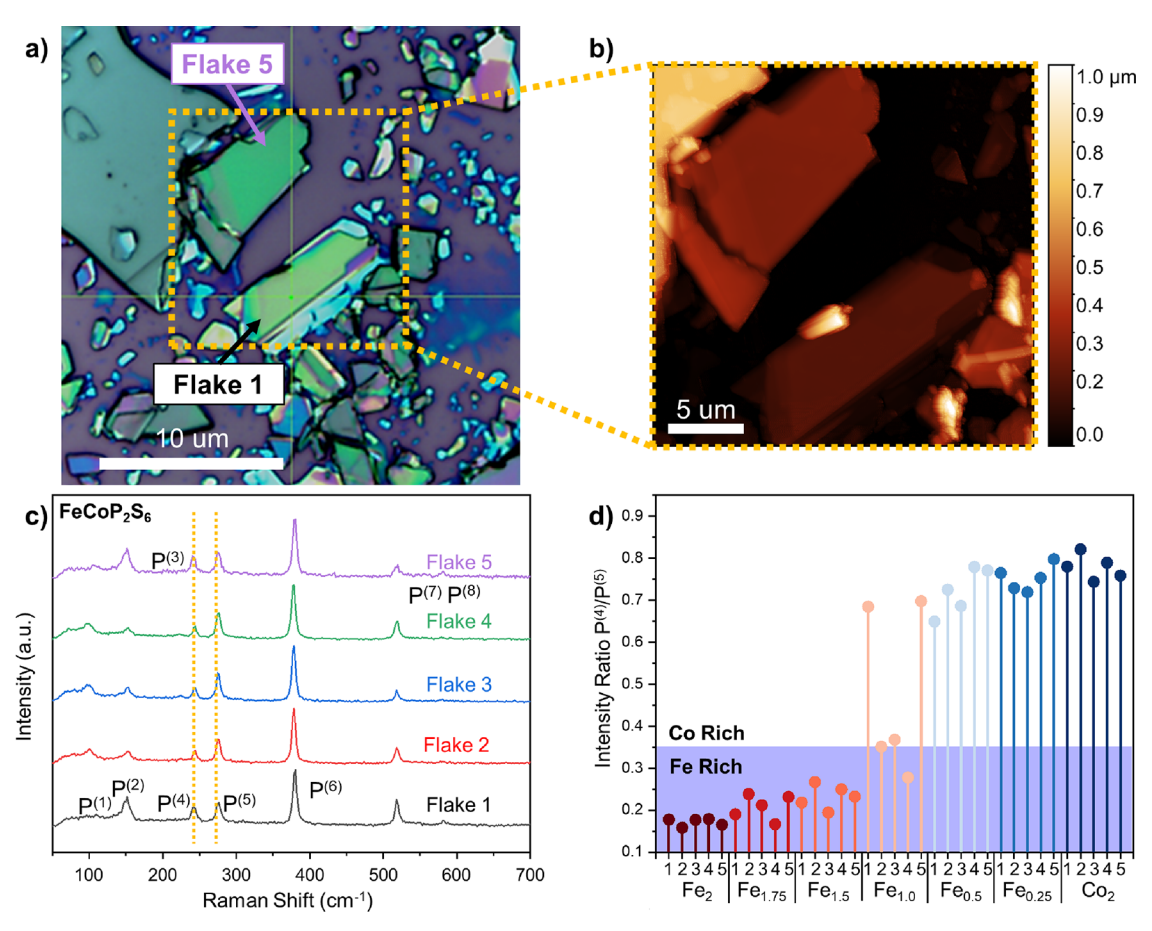


Figure 3. (a) Optical image of representative flakes with Flakes 1 and 5 from the exfoliated FeCoP<sub>2</sub>S<sub>6</sub> sample indicated. The green crosshair indicates the current position of the laser before taking the measurement. In this case, it is positioned over Flake 1. (b) Corresponding AFM image for Flakes 1 and 5. (c) Raman spectra for the five flakes of interest for FeCoP<sub>2</sub>S<sub>6</sub>. (d) Calculated intensity ratio  $P^4/P^{(5)}$  for five flakes of interest for all Fe<sub>2-x</sub>Co<sub>x</sub>P<sub>2</sub>S<sub>6</sub> (x = 0-2). Due to the limit of space, only the Fe composition is indicated except for Co<sub>2</sub>P<sub>2</sub>S<sub>6</sub>.

Co ions should be considered to have a 2+ charge to retain charge neutrality. This is in accordance with the SEM-EDS findings.

The Mössbauer spectra become more interesting when measured at 77 K, which is below the antiferromagnetic ordering temperature,  $T_{\rm N\acute{e}el}$  of both Fe<sub>2</sub>P<sub>2</sub>S<sub>6</sub> ( $T_{\rm N\acute{e}el}$  = 123 K) and Co<sub>2</sub>P<sub>2</sub>S<sub>6</sub> ( $T_{\rm N\acute{e}el}$  = 120). The magnetic interactions between adjacent Fe<sup>2+</sup> and Co<sup>2+</sup> cations are manifested in the shape of the Mössbauer spectra where the composition plays a dominant role (Figure 2b). For low levels of alloying as in the cases of  $Fe_{1.75}Co_{0.25}P_2S_6$  and  $Fe_{1.5}Co_{0.5}P_2S_6$ , the spectra are dominated by a main narrow resonant line component (M1blue), which is represented by the blue curve in the fitted spectra, with Mössbauer parameters (Table S4) similar to that of the monometallic Fe<sub>2</sub>P<sub>2</sub>S<sub>6</sub> system. There is also an additional Fe2+ component (M2-red) with broader resonant lines and different Mössbauer parameters, represented by the red fitted curve, that evolves as the Co alloying increases. However, an interesting behavior is observed when the Fe/Co ratio is equal at FeCoP<sub>2</sub>S<sub>6</sub>. The shape of the spectrum for this sample changes dramatically toward significantly broader resonant lines. When applying a fitting model with two components, the M2 component is now the dominant contributing component, which acquires the majority of the absorption area that reaches an M2/M1 ratio of 80/20, as compared to the M2/M1 ratio of 30/70 observed for the corresponding spectrum of the Fe<sub>1.5</sub>Co<sub>0.5</sub>P<sub>2</sub>S<sub>6</sub> sample. With

increasing Co content, the M2 component develops an even higher hyperfine magnetic field,  $B_{\rm hf}^{\ C}$ , as can be seen for  ${\rm Fe_{0.5}Co_{1.5}P_2S_6}$  and  ${\rm Fe_{0.25}Co_{1.75}P_2S_6}$  samples in Table S4, compared to  ${\rm FeCoP_2S_6}$ . It is also interesting to note here that the  $B_{\rm hf}^{\ C}$  for component M1 is rather consistent in all measured samples and only exhibits small shifts in comparison. Furthermore, there is a substantial asymmetric broadening in the resonant lines for component M2 relative to that for M1, while the absorption area ratio remains nearly constant at an M2/M1 of  $\sim$ 80/20.

According to these results, it is reasonable to conclude that the M1 and M2 components correspond approximately to two groups of Fe2+ ions in the alloyed Fe2-xCoxP2S6 system. If a random distribution of Co ions in the structure is assumed, where Co does not have a preferred site, then each FeS<sub>6</sub> octahedron in any given monolayer will share edges with three FeS<sub>6</sub> or CoS<sub>6</sub> octahedra. Taking into account the Co composition, a simple statistical model based on a binomial distribution can give the probabilities of a FeS<sub>6</sub> octahedron sharing common edges with no CoS<sub>6</sub> and three FeS<sub>6</sub>, one CoS<sub>6</sub> and two FeS<sub>6</sub>, two CoS<sub>6</sub> and one FeS<sub>6</sub>, or three CoS<sub>6</sub> and no FeS<sub>6</sub> octahedra (Table S5). Relating roughly the values of these probabilities to the values of the absorption areas of components M1 and M2, it seems that component M1 corresponds to the Fe2+ cations, which are in octahedra having a majority of other FeS<sub>6</sub> octahedra attached to them (three or two  $FeS_6$ ), while component M2 corresponds to the  $Fe^{2+}$  ions

in octahedra having a majority of other  $CoS_6$  octahedra attached to them (two or three  $CoS_6$ ). Thus, it can be concluded that the clustering of Co cations in the Co-rich areas containing some significant parts of Fe cations in the layered structures in the  $Fe_{2-x}Co_xP_2S_6$  systems is already attained when the Fe/Co ratio is 1:1 at  $FeCoP_2S_6$ . Where above this threshold, the Co-rich regions will likely host constant concentrations of Fe ions. Within the Fe-rich areas, a relatively constant Fe-Co stoichiometry is maintained.

3.3. Raman Analysis on Exfoliated Samples. To evaluate the composition of Fe<sub>2-x</sub>Co<sub>x</sub>P<sub>2</sub>S<sub>6</sub> in thinned samples on the order of a few hundred nanometers in thickness, bulk crystals are mechanically exfoliated by the scotch tape method and deposited onto silicon wafers with a thermal oxide layer for analysis. Raman spectroscopy is a powerful tool to fingerprint Fe<sub>2-x</sub>Co<sub>x</sub>P<sub>2</sub>S<sub>6</sub>. As previously reported by Cheng et al., a distinct change in the relative intensity ratios of designated peaks in the Raman spectra of  $Fe_{2-x}Co_xP_2S_6$  as the alloying ratio of Fe:Co is increased or decreased. These designated peaks at ~150,  $\sim$ 245, $\sim$ 275, and  $\sim$ 380 cm<sup>-1</sup> are labeled as peaks P<sup>1</sup>, P<sup>4</sup>, P<sup>5</sup>, and P<sup>6</sup>, respectively (Figure S5a). An inverse relationship between the intensity ratios  $P^{(6)}(\sim 380 \text{ cm}^{-1})/P^{(1)}(\sim 150 \text{ cm}^{-1})$  and  $P^{(4)}(\sim 245 \text{ cm}^{-1})/P^{(5)}(\sim 275 \text{ cm}^{-1})$  is apparent as increasing the Co content  $P^4/P^{(5)}$  will increase while  $P^6/P^{(1)}$  will decrease. In this study, the intensity ratio  $P^4/P^{(5)}$  is used to determine the stoichiometry of the exfoliated flakes.

With the synthesis of two additional systems, Fe<sub>1.5</sub>Co<sub>0.5</sub>P<sub>2</sub>S<sub>6</sub> and Fe<sub>0.5</sub>Co<sub>1.5</sub>P<sub>2</sub>S<sub>6</sub>, the bulk samples of all alloyed  $Fe_{2-x}Co_xP_2S_6$  (0, 0.25, 0.5, 1.0, 1.5, 1.75, and 2) are evaluated, as shown in Figure S5a. As the Co content increases, there is a clear rise in the intensity of  $P^{(4)}$  and a decrease in the intensity of P5. Plotting the intensity ratio P4/P(5) as a function of  $Fe_{2-x}Co_xP_2S_6$  as x is varied, and it can be observed that there are two separate linear regimes denoted by a solid line from x= 0 to 1.0 and a dotted line from x = 1.0 to 2.0 (Figure S5b). This is in contrast to what was previously reported where a single linear trend was apparent.26 However, this can be attributed to considering fewer alloyed samples of Fe<sub>2-x</sub>Co<sub>x</sub>P<sub>2</sub>S<sub>6</sub>, where in this current study, Fe<sub>1.5</sub>Co<sub>0.5</sub>P<sub>2</sub>S<sub>6</sub> and Fe<sub>0.5</sub>Co<sub>1.5</sub>P<sub>2</sub>S<sub>6</sub> are also included. Further alloyed samples will give a more precise relationship between the composition and the intensity ratios. However, it is still consistent that a higher Co concentration will be correlated with an increase in the P<sup>4</sup>/ P<sup>(5)</sup> intensity ratio.

Five flakes from each respective  $Fe_{2-x}Co_xP_2S_6$  (x = 0-2) system were chosen at random for Raman analysis. Representative flakes from the exfoliated FeCoP<sub>2</sub>S<sub>6</sub> sample are shown in Figure 3a with an accompanying tapping atomic force microscopy (AFM) image of the same flakes shown in Figure 3b. Two flakes of interest are labeled as Flakes 1 and 5. The green crosshairs indicate where the laser position was prior to measurement. In this case, it is positioned on Flake 1. The normalized Raman spectra for the five flakes of FeCoP<sub>2</sub>S<sub>6</sub> are shown in Figure 3c. All peaks are normalized to the tallest peak P<sup>6</sup>. Also note that the peak at 520 cm<sup>-1</sup> is a contribution from the silicon substrate. It is immediately apparent that the Raman spectra for Flakes 1 and 5 are different from Flakes 2, 3, and 4. Both Flakes 1 and 5 have P<sup>(4)</sup> and P<sup>(5)</sup> peaks of similar intensities, while Flakes 2, 3, and 4 have a much more intense  $P^{(5)}$  peak relative to  $P^4$ . An identical treatment is carried out on the other  $Fe_{2-x}Co_xP_2S_6$  samples (x = 0, 0.25, 0.5, 1.5, 1.75, and2.0), and the  $P^4/P^{(5)}$  intensity ratio for the five flakes for each  $Fe_{2-x}Co_xP_2S_6$  system is shown in Figure 3d. The graph is

divided between the Fe-rich region, denoted in the shaded portion of the graph, and the Co-rich region. Within each cluster of the five flakes for each  $Fe_{2-x}Co_xP_2S_6$  system (x = 0, 0.25, 0.5, 1.5, 1.75, and 2.0), there is a small variation in the composition of each respective flake. Thus, some exfoliated flakes have a higher or lower Fe:Co ratio than expected. However, in the case of FeCoP<sub>2</sub>S<sub>6</sub>, it is clear that Flakes 1 and 5 are substantially more Co-rich while Flakes 2, 3, and 4 are closer to the expected composition of 1:1 Fe:Co. Tapping AFM maps for  $Fe_{2-x}Co_xP_2S_6$  systems (x = 0.25, 0.5, 1.0, 1.5,and 1.75) (Figure S7-S11) indicates that the composition variations occur on length scales of a few hundred nanometers. For example, in the case of FeCoP<sub>2</sub>S<sub>6</sub>, Flake 1 is 267 nm thick while Flake 4 is 223 nm thick (Figure S9). The conclusion that can be drawn here is that the Fe<sub>2-x</sub>Co<sub>x</sub>P<sub>2</sub>S<sub>6</sub> system is not an atomically homogeneous solid solution with a much greater tendency to coalesce into Fe-rich and Co-rich regions that can span hundreds of nanometers in thickness when the bulk Fe:Co ratio approaches 1:1.

It should be noted that for the Fe-rich samples  $(Fe_{2-x}Co_xP_2S_6, x = 0, 0.25, and 0.5)$ , the clustering of the P<sup>4</sup>/P<sup>(5)</sup> intensity ratio increases with increasing Co concentration. Similarly, in the Co-rich samples (Fe<sub>2-x</sub>Co<sub>x</sub>P<sub>2</sub>S<sub>6</sub>, x =1.5, 1.75, and 2.0), the clustering of the  $P^4/P^{(5)}$  intensity ratio increases with increasing Co content. Taking the average of all five flakes for each respective system, it can be seen that the average P<sup>4</sup>/P<sup>(5)</sup> intensity ratio does increase with increasing Co concentration (Table S6). This is consistent with our bulk analysis as each individual exfoliated flake was once a part of a bulk crystal of  $Fe_{2-x}Co_xP_2S_6$ . It should be noted here that there is a larger spread in the  $P^4/P^{(5)}$  intensity ratio for the five flakes for Co<sub>2</sub>P<sub>2</sub>S<sub>6</sub> as compared with Fe<sub>2</sub>P<sub>2</sub>S<sub>6</sub>. Co<sub>2</sub>P<sub>2</sub>S<sub>6</sub> has a standard deviation of 0.03, and Fe<sub>2</sub>P<sub>2</sub>S<sub>6</sub> has a standard deviation of 0.01 (Table S6). This indicates that there will be greater uncertainty in correlating the  $P^4/P^{(5)}$  intensity ratio with the composition at higher Co concentrations and should be considered. To corroborate all these results, we performed SEM-EDS measurements on each flake for all the alloyed Fe2-xCoxP2S6 systems (x = 0.25, 0.5, 1.0, 1.5,and 1.75), as shown in Figure S6, and a similar trend is observed as in the plot of the  $P^4/P^{(5)}$ intensity ratio shown in Figure 3d. The composition is determined by the same treatment as described in Section 3.1 where the Fe<sub>2</sub>P<sub>2</sub>S<sub>6</sub> sample is used as a calibration sample.

3.4. EELS Analysis. Continuing with the top-down structural and stoichiometric analysis of the Fe2-xCoxP2S6 system, scanning transmission electron microscopy (STEM) is used to interrogate thin exfoliated flakes of selected members of the  $Fe_{2-x}Co_xP_2S_6$  system (x = 0.25, 1.0, and 1.75) at nanometer resolution. EELS is a powerful tool that can be used for elemental chemical mapping at the desired resolution at the nanoscale. Using EELS, the lateral distribution of Fe and Co is evaluated within a surface area of  $5 \times 5$  nm<sup>2</sup>. For comparison purposes, two separate regions, one thinner and one thicker, were considered for each system. High-angle annular dark-field (HAADF) images for a thin region (Figure 4b) and thicker region (Figure 4c) for exfoliated FeCoP<sub>2</sub>S<sub>6</sub> indicate where each corresponding core-loss spectra (Figure 4d) is measured. The thicknesses of the thin and thick regions are evaluated using the low-loss EELS spectra taken from each respective region (Figure S12). From Figure S12, a clear rise in the plasmon peak (~20 eV) indicates a much thicker area. Using the logratio method described by Malis et al., the thicknesses of the two regions are found to be 11 and 51 nm, respectively.<sup>34</sup>

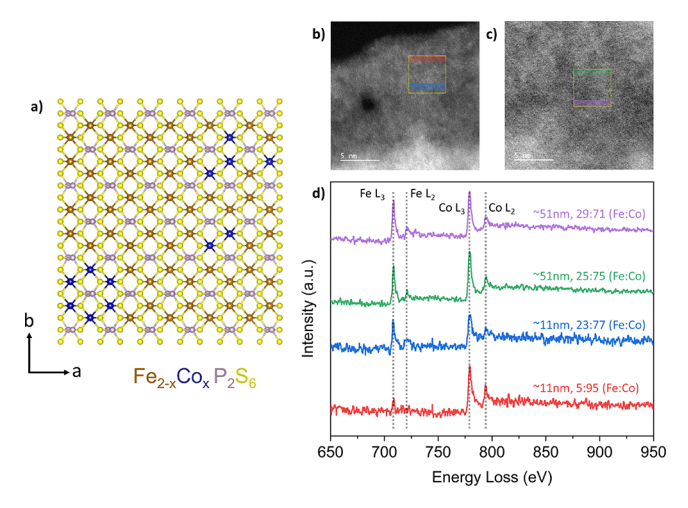


**Figure 4.** (a) Schematic of potential Co clustering within a single layer of  $Fe_{2-x}Co_xP_2S_6$ . (b) HAADF image of the thin region in the flake of interest with sample areas marked in red and blue. The region of interest is approximately 11 nm thick. (c) HAADF image of the thicker region in the flake of interest with sample areas marked in green and purple. The region of interest is approximately 51 nm thick. (d) Core-loss EELS for thin and thick regions of the flake of interest with red, blue, green, and purple spectra corresponding to red, blue, green, and purple regions marked in panels (b, c), respectively.

The Fe-L<sub>3</sub> edge is at 708 eV, while the Co-L<sub>3</sub> edge is at 779 eV. From Figure 4d, both the Fe-edge and the Co-edge with respective white lines are observed in all four spectra. However, in the red spectra, which correspond to the red region, in Figure 4c, the Fe-edge and associated white lines are drastically suppressed compared to the Co-edge. Using Fe<sub>2</sub>P<sub>2</sub>S<sub>6</sub> and Co<sub>2</sub>P<sub>2</sub>S<sub>6</sub> core-loss spectra (Figure S13) as reference spectra, the composition of each region (red, blue, green, and purple; all  $5 \times 1 \text{ nm}^2$ ) is evaluated from the spectra in Figure 4 using DigitalMicrograph.<sup>35</sup> The expected composition is 50:50 Fe:Co for FeCoP<sub>2</sub>S<sub>6</sub>. However, it can be observed that all four spectra deviate from this composition ratio. The blue, green, and purple spectra correspond to a composition of 25:75 Fe:Co, and the red curve corresponds to an exceedingly Co-rich region where the composition is 5:95. Comparing the composition of the  $5 \times 5 \times \sim 11$  nm<sup>3</sup> region versus the  $5 \times 5 \times$  $\sim$ 51 nm<sup>3</sup> region for FeCoP<sub>2</sub>S<sub>6</sub> in Figure S14, the 51 nm-thick region has a composition closer to 30:70 while the thin region has a composition of 25:75 Fe:Co. A few distinct conclusions can be made. The composition of this flake that was exfoliated from bulk FeCoP<sub>2</sub>S<sub>6</sub> is closer to 30:70 Fe:Co instead of 50:50, which is consistent with the findings of the Raman analysis on exfoliated flakes where the composition variation occurs within flakes that are a few hundred nanometers thick. Also, there is a clear segregation of Co into a predominantly Co-rich region within a  $5 \times 5 \times \sim 11$  nm<sup>3</sup> region of the sample, indicating that there are likely intralayer composition variations and interlayer differences, as shown schematically in Figure 4a.

The same treatment to determine composition and thickness is conducted on flakes exfoliated from  $Fe_{1.75}Co_{0.25}P_2S_6$  and  $Fe_{0.25}Co_{1.75}P_2S_6$  to determine the behavior of the composition variations at the extremes of the alloying compositions. The thickness is determined from low-loss EELS (Figure S12) and  $Fe_2P_2S_6$  and  $Co_2P_2S_6$  spectra used as reference (Figure S13). From Figure S15, the flake exfoliated from  $Fe_{1.75}Co_{0.25}P_2S_6$  shows all four spectra with nearly identical compositions with a slight deviation from the

expected composition of 7:1 Fe:Co with composition ratios closer to 80:20 Fe:Co in  $\sim\!15$  and  $\sim\!33$  nm regions. In contrast, from Figure S16, the flake exfoliated from Fe $_{0.25}\text{Co}_{1.75}\text{P}_2\text{S}_6$  shows all four spectra with compositions closest to the expected composition of 1:7 Fe:Co with only small deviations from the expected compositions of 1:7 in both the  $\sim\!18$  and  $\sim\!77$  nm-thick regions.

#### 4. SUMMARY AND CONCLUSIONS

A thorough study of the structural and chemical compositions of  $Fe_{2-x}Co_xP_2S_6$  (x = 0, 0.25, 0.5, 1.0, 1.5, 1.75, and 2.0) was evaluated as a continuation from a previous publication on the Fe<sub>2-x</sub>Co<sub>x</sub>P<sub>2</sub>S<sub>6</sub>. 26 Structural analysis by pXRD on bulk samples of Fe<sub>2-x</sub>Co<sub>x</sub>P<sub>2</sub>S<sub>6</sub> confirms that all alloyed thiophosphate samples are C2/m with increasing Co stoichiometry, leading to a smaller average unit cell as expected. Compositional analysis with SEM-EDS on bulk samples corroborates the expected stoichiometry of the alloyed samples. Room temperature Mössbauer spectroscopy measurements indicate that that there is a negligible alteration in the local or global crystal structure with changing the alloying ratio of Fe/Co. There are also negligible cation vacancies present in the lattice as Fe cations are replaced with Co cations, which in turn indicates that both metal cations species are of a 2+ charge. When the samples are cooled to 77 K, the Mössbauer spectroscopy measurements become sensitive to the cation magnetic ordering within the lattice. They indicate the presence of Ferich and Co-rich regions of consistent compositions. This was confirmed by conducting a Raman analysis on randomly selected exfoliated flakes of  $Fe_{2-x}Co_xP_2S_6$  (x = 0, 0.25, 0.5, 1.0,1.5, 1.75, and 2.0). These measurements determined that flakes up to ~250 nm in thickness already show fluctuations in Fe/ Co alloying, with the largest variation being observed in FeCoP<sub>2</sub>S<sub>6</sub>. Bringing the analysis to an even higher resolution, STEM-EELS is used to determine that within a 5 nm by 5 nm area flake exfoliated from bulk FeCoP2S6, a completely Fedeficient region is observed. This further highlights the potential for composition variations on multiple length scales when conducting studies with alloyed chalcophosphate systems. This work provides insight into engineering the chalcophosphates for specific applications such as when used in conjunction with other 2D materials for next-generation nanoelectronic devices. Our findings call for further research on alloyed chalcophosphates, with an emphasis on care being applied when interpreting data from solid solutions and designing high entropy alloy chalcophosphates as potential compositional changes may occur at multiple length scales and greatly impact the expected properties.

#### ASSOCIATED CONTENT

## Supporting Information

The Supporting Information is available free of charge at https://pubs.acs.org/doi/10.1021/acs.chemmater.2c03738.

Experimental and physical property measurements; pXRD refinements and supplementary SEM-EDS measurements of bulk  $Fe_{2-x}Co_xP_2S_6$  samples; supplementary Mössbauer spectra at RT with a wider velocity range and tables of Mössbauer constants; supplementary Raman spectra on bulk  $Fe_{2-x}Co_xP_2S_6$  samples; supplementary SEM-EDS on exfoliated samples with AFM maps and profiles; supplementary LL-EELS for

 $Fe_{2-x}Co_xP_2S_6$  (x = 0.25, 1.00, and 1.75); and core-loss EELS for  $Fe_{2-x}Co_xP_2S_6$  (x = 0.25 and 1.75) (PDF)

### AUTHOR INFORMATION

#### **Corresponding Author**

Vinayak P. Dravid — Department of Material Science and Engineering, Northwestern University Atomic and Nanoscale Characterization Experimental (NUANCE) Center, and International Institute for Nanotechnology (IIN), Northwestern University, Evanston, Illinois 60208, United States; orcid.org/0000-0002-6007-3063; Email: v-dravid@northwestern.edu

#### **Authors**

Matthew Cheng — Department of Material Science and Engineering, Northwestern University, Evanston, Illinois 60208, United States; Occid.org/0000-0002-1062-5974

Abishek K. Iyer — Department of Chemistry, Northwestern University, Evanston, Illinois 60208, United States; orcid.org/0000-0002-8582-3895

Alexios P. Douvalis – Department of Physics, University Research Center of Ioannina, Ioannina 451 10, Greece

Stephanie M. Ribet — Department of Material Science and Engineering and International Institute for Nanotechnology (IIN), Northwestern University, Evanston, Illinois 60208, United States; ocid.org/0000-0002-7117-066X

Mercouri G. Kanatzidis — Department of Chemistry, Northwestern University, Evanston, Illinois 60208, United States; © orcid.org/0000-0003-2037-4168

Complete contact information is available at: https://pubs.acs.org/10.1021/acs.chemmater.2c03738

#### Notes

The authors declare no competing financial interest.

## ACKNOWLEDGMENTS

This work was supported by NSF Division of Material Research (grants DMR-1929356 and DMR-2003476). This work made use of the EPIC facility of Northwestern University's NUANCE Center, which has received support from the SHyNE Resource [National Science Foundation (NSF) grant ECCS-2025633, Northwestern's MRSEC program (NSF grant DMR-1720139), the Keck Foundation, and the State of Illinois through IIN. The materials synthesis in this work was partially supported by the Army Research Office (grant W911NF1910335). M.C. acknowledges support from the NSF Graduate Research Fellowship under grant DGE-1842165. A.K.I. and M.G.K. acknowledge the Air Force Office of Scientific Research grant number FA9550-18-S-0003. S.M.R. acknowledges support from the IIN Ryan Fellowship, the 3 M Northwestern Graduate Research Fellowship, and the Department of Energy Office of Science Graduate Student Research fellowship program. All figures of crystal structures were produced by VESTA.<sup>36</sup>

#### REFERENCES

- (1) Novoselov, K. S.; Fal'ko, V. I.; Colombo, L.; Gellert, P. R.; Schwab, M. G.; Kim, K. A Roadmap for Graphene. *Nature* **2012**, 490, 192–200
- (2) Nicolosi, V.; Chhowalla, M.; Kanatzidis, M. G.; Strano, M. S.; Coleman, J. N. Liquid Exfoliation of Layered Materials. *Science* **2013**, 340, No. 1226419.

- (3) Wang, Q. H.; Kalantar-Zadeh, K.; Kis, A.; Coleman, J. N.; Strano, M. S. Electronics and Optoelectronics of Two-Dimensional Transition Metal Dichalcogenides. *Nat. Nanotechnol.* **2012**, *7*, 699–712
- (4) Wang, F.; Shifa, T. A.; Yu, P.; He, P.; Liu, Y.; Wang, F.; Wang, Z.; Zhan, X.; Lou, X.; Xia, F.; He, J. New Frontiers on van Der Waals Layered Metal Phosphorous Trichalcogenides. *Adv. Funct. Mater.* **2018**, 28, No. 1802151.
- (5) Susner, M. A.; Chyasnavichyus, M.; McGuire, M. A.; Ganesh, P.; Maksymovych, P. Metal Thio- and Selenophosphates as Multifunctional van Der Waals Layered Materials. *Adv. Mater.* **2017**, 29, No. 1602852.
- (6) Butler, S. Z.; Hollen, S. M.; Cao, L.; Cui, Y.; Gupta, J. A.; Gutiérrez, H. R.; Heinz, T. F.; Hong, S. S.; Huang, J.; Ismach, A. F.; Johnston-Halperin, E.; Kuno, M.; Plashnitsa, V. V.; Robinson, R. D.; Ruoff, R. S.; Salahuddin, S.; Shan, J.; Shi, L.; Spencer, M. G.; Terrones, M.; Windl, W.; Goldberger, J. E. Progress, Challenges, and Opportunities in Two-Dimensional Materials Beyond Graphene. *ACS Nano* 2013, 7, 2898–2926.
- (7) Coleman, J. N.; Lotya, M.; O'Neill, A.; Bergin, S. D.; King, P. J.; Khan, U.; Young, K.; Gaucher, A.; De, S.; Smith, R. J.; Shvets, I. V.; Arora, S. K.; Stanton, G.; Kim, H.-Y.; Lee, K.; Kim, G. T.; Duesberg, G. S.; Hallam, T.; Boland, J. J.; Wang, J. J.; Donegan, J. F.; Grunlan, J. C.; Moriarty, G.; Shmeliov, A.; Nicholls, R. J.; Perkins, J. M.; Grieveson, E. M.; Theuwissen, K.; McComb, D. W.; Nellist, P. D.; Nicolosi, V. Two-Dimensional Nanosheets Produced by Liquid Exfoliation of Layered Materials. *Science* 2011, 331, 568–571.
- (8) Mayorga-Martinez, C. C.; Sofer, Z.; Sedmidubský, D.; Huber, Š.; Eng, A. Y. S.; Pumera, M. Layered Metal Thiophosphite Materials: Magnetic, Electrochemical, and Electronic Properties. *ACS Appl. Mater. Interfaces* **2017**, *9*, 12563–12573.
- (9) Long, M.; Shen, Z.; Wang, R.; Dong, Q.; Liu, Z.; Hu, X.; Hou, J.; Lu, Y.; Wang, F.; Zhao, D.; Ding, F.; Tu, Y.; Han, T.; Li, F.; Zhang, Z.; Hou, X.; Wang, S.; Shan, L. Ultrasensitive Solar-Blind Ultraviolet Photodetector Based on FePSe <sub>3</sub> /MoS <sub>2</sub> Heterostructure Response to 10.6 Mm. *Adv. Funct. Mater.* **2022**, *32*, No. 2204230.
- (10) Si, M.; Liao, P.-Y.; Qiu, G.; Duan, Y.; Ye, P. D. Ferroelectric Field-Effect Transistors Based on MoS2 and CuInP2S6 Two-Dimensional van Der Waals Heterostructure. *ACS Nano* **2018**, *12*, 6700–6705.
- (11) Ouvrard, G.; Brec, R.; Rouxel, J. Structural Determination of Some MPS3 Layered Phases (M = Mn, Fe, Co, Ni and Cd). *Mater. Res. Bull.* **1985**, *20*, 1181–1189.
- (12) Chica, D. G.; Iyer, A. K.; Cheng, M.; Ryan, K. M.; Krantz, P.; Laing, C.; dos Reis, R.; Chandrasekhar, V.; Dravid, V. P.; Kanatzidis, M. G. P  $_2$  S  $_5$  Reactive Flux Method for the Rapid Synthesis of Monoand Bimetallic 2D Thiophosphates M  $_{2-x}$  M $'_x$  P  $_2$  S  $_6$ . Inorg. Chem. **2021**, 60, 3502–3513.
- (13) Joy, P. A.; Vasudevan, S. Magnetism in the Layered Transition-Metal Thiophosphates M PS 3 (M =Mn, Fe, and Ni). *Phys. Rev. B* **1992**, 46, 5425–5433.
- (14) Murayama, C.; Okabe, M.; Urushihara, D.; Asaka, T.; Fukuda, K.; Isobe, M.; Yamamoto, K.; Matsushita, Y. Crystallographic Features Related to a van Der Waals Coupling in the Layered Chalcogenide FePS 3. J. Appl. Phys. 2016, 120, 142114.
- (15) Checa, M.; Ivanov, I.; Neumayer, S. M.; Susner, M. A.; McGuire, M. A.; Maksymovych, P.; Collins, L. Correlative Piezoresponse and Micro-Raman Imaging of CuInP <sub>2</sub> S <sub>6</sub> -In <sub>4/3</sub> P <sub>2</sub> S <sub>6</sub> Flakes Unravels Phase-Specific Phononic Fingerprint via Unsupervised Learning. *Appl. Phys. Lett.* **2022**, *121*, No. 062901.
- (16) Shannon, R. D. Revised Effective Ionic Radii and Systematic Studies of Interatomic Distances in Halides and Chalcogenides. *Acta Crystallogr., Sect. A* **1976**, 32, 751–767.
- (17) Ouili, Z.; Leblanc, A.; Colombet, P. Crystal Structure of a New Lamellar Compound. *J. Solid State Chem.* **1987**, *66*, 86–94.
- (18) Shemerliuk, Y.; Zhou, Y.; Yang, Z.; Cao, G.; Wolter, A. U. B.; Büchner, B.; Aswartham, S. Tuning Magnetic and Transport Properties in Quasi-2D (Mn1–xNix)2P2S6 Single Crystals. *Electron. Mater.* **2021**, *2*, 284–298.

**Chemistry of Materials** Article pubs.acs.org/cm

- (19) Ying, T.; Yu, T.; Qi, Y.; Chen, X.; Hosono, H. High Entropy van Der Waals Materials. Adv. Sci. 2022, No. 2203219.
- (20) Ying, T.; Yu, T.; Shiah, Y.-S.; Li, C.; Li, J.; Qi, Y.; Hosono, H. High-Entropy van Der Waals Materials Formed from Mixed Metal Dichalcogenides, Halides, and Phosphorus Trisulfides. J. Am. Chem. Soc. 2021, 143, 7042-7049.
- (21) Wang, R.; Huang, J.; Zhang, X.; Han, J.; Zhang, Z.; Gao, T.; Xu, L.; Liu, S.; Xu, P.; Song, B. Two-Dimensional High-Entropy Metal Phosphorus Trichalcogenides for Enhanced Hydrogen Evolution Reaction. ACS Nano 2022, No. acsnano.2c01064.
- (22) Zhang, X.; Su, X.; Chen, X.; Qin, J.; Inokuchi, M. The Synthesis and Magnetism of Mixed Metal Hexathiohypodiphosphate (MnxCd1-xPS3) System and Its Intercalates. Microporous Mesoporous Mater. 2008, 108, 95-102.
- (23) Masubuchi, T.; Hoya, H.; Watanabe, T.; Takahashi, Y.; Ban, S.; Ohkubo, N.; Takase, K.; Takano, Y. Phase Diagram, Magnetic Properties and Specific Heat of Mn1-xFexPS3. J. Alloys Compd. 2008, 460, 668-674.
- (24) Takano, Y.; Arai, A.; Takahashi, Y.; Takase, K.; Sekizawa, K. Magnetic Properties and Specific Heat of New Spin Glass Mn0.5Fe0.5PS3. J. Appl. Phys. 2003, 93, 8197–8199.
- (25) Checa, M.; Jin, X.; Millan-Solsona, R.; Neumayer, S. M.; Susner, M. A.; McGuire, M. A.; O'Hara, A.; Gomila, G.; Maksymovych, P.; Pantelides, S. T.; Collins, L. Revealing Fast Cu-Ion Transport and Enhanced Conductivity at the CuInP 2 S 6 -In 4/3 P  $_2$  S  $_6$  Heterointerface. ACS Nano 2022, 16, 15347–15357.
- (26) Cheng, M.; Lee, Y.-S.; Iyer, A. K.; Chica, D. G.; Qian, E. K.; Shehzad, M. A.; dos Reis, R.; Kanatzidis, M. G.; Dravid, V. P. Mixed Metal Thiophosphate Fe 2-x Co x P 2 S 6: Role of Structural Evolution and Anisotropy. Inorg. Chem. 2021, 60, 17268-17275.
- (27) Douvalis, A. P.; Polymeros, A.; Bakas, T. IMSG09: A 57 Fe- 119 Sn Mössbauer Spectra Computer Fitting Program with Novel Interactive User Interface. J. Phys. Conf. Ser. 2010, 217, No. 012014.
- (28) Sakai, H.; Ukita, R.; Machida, N.; Shigematsu, T. X-Ray Diffraction and Mössbauer Spectroscopic Studies of FePS 3 -Alkylamines Intercalation Compounds. Bull. Chem. Soc. Jpn. 1999, 72, 2249-2252.
- (29) Ehm, L.; Vogel, S.; Knorr, K.; Schmid-Beurmann, P.; Depmeier, W. X-Ray Powder Diffraction and 57Fe Mössbauer Spectroscopy Study on Fe0.47NbS2. J. Alloys Compd. 2002, 339, 30-34.
- (30) DiSalvo, F. J.; Eibschutz, M.; Cros, C.; Murphy, D. W.; Waszczak, J. V. Magnetic and Mössbauer Studies of Li x M y V 1-yS 2 (M = Fe or Cr). Phys. Rev. B 1979, 19, 3441-3448.
- (31) Wildes, A. R.; Simonet, V.; Ressouche, E.; Ballou, R.; McIntyre, G. J. The Magnetic Properties and Structure of the Quasi-Two-Dimensional Antiferromagnet CoPS3. J. Phys. Condens. Matter 2017, 29, 455801.
- (32) Ban, S.; Takano, Y.; Ohkubo, N.; Hoya, H.; Takahashi, Y.; Takase, K.; Sekizawa, K. Mössbauer Study of the Transition Metal Phosphorus Trichalcogenide FePS3 and Spin Glass Mn0.5Fe0.5PS3. Hyperfine Interact. 2005, 165, 95-99.
- (33) Fatseas, G. A.; Evain, M.; Ouvrard, G.; Brec, R.; Whangbo, M.-H. Unusual Mössbauer Phenomenon in Li x FePS 3. Phys. Rev. B 1987, 35, 3082-3087.
- (34) Malis, T.; Cheng, S. C.; Egerton, R. F. EELS Log-Ratio Technique for Specimen-Thickness Measurement in the TEM. J. Electron Microsc. Technol. 1988, 8, 193-200.
- (35) DigitalMicrograph; GATAN, Inc.: Pleasanton, CA, US.
- (36) Momma, K.; Izumi, F. VESTA 3 for Three-Dimensional Visualization of Crystal, Volumetric and Morphology Data. J. Appl. Crystallogr. 2011, 44, 1272-1276.

## **□** Recommended by ACS

## **Enhanced Oxide Ion Conductivity by Ta Doping of** Ba<sub>3</sub>Nb<sub>1-x</sub>Ta<sub>x</sub>MoO<sub>8.5</sub>

Brent Sherwood, Abbie C. Mclaughlin, et al.

IANIIARY 17 2023 INORGANIC CHEMISTRY

READ 2

**Preparation and Characterization of Francisite Solid** Solutions  $Cu_3Bi(Se_{1-x}Te_xO_3)_2O_2Br$  (x = 0-1): Possibility for Francisites as Starting Materials for Oxide van der Waa...

Maria Markina, Alexander Vasiliev, et al.

DECEMBER 30, 2022

CHEMISTRY OF MATERIALS

READ M

**Structural Complexity and Tuned Thermoelectric Properties** of a Polymorph of the Zintl Phase Ca<sub>2</sub>CdSb<sub>2</sub> with a Noncentrosymmetric Monoclinic Structure

Michael O. Ogunbunmi, Svilen Bobev, et al.

JULY 07, 2022

INORGANIC CHEMISTRY

READ **C** 

#### Tunable Salt-Inclusion Chalcogenides for Ion Exchange, Photoluminescence, and Scintillation

Anna A. Berseneva, Hans-Conrad zur Loye, et al.

JANUARY 23, 2023

CHEMISTRY OF MATERIALS

RFAD 🗹

Get More Suggestions >